ACSNANO

www.acsnano.org

ARTICLE

Rapid Prediction of Bimetallic Mixing Behavior at the Nanoscale

James Dean,[†] Michael J. Cowan,[†] Jonathan Estes, Mahmoud Ramadan, and Giannis Mpourmpakis*

Cite This: *ACS Nano* 2020, 14, 8171−8180

Read Online

ACCESS | Metrics & More | Article Recommendations | Supporting Information

ABSTRACT: The nanoparticle (NP) design space allows for variations in size, shape, composition, and chemical ordering. In the search for low-energy structures, this results in an extremely large search space which cannot be screened by brute force methods. In this work, we develop a genetic algorithm to predict stable bimetallic NPs of any size, shape, and metal composition. Our method predicts nanostructures in agreement with experimental trends and it captures the detailed chemical ordering of an experimental 23,196-atom FePt NP with nearly atom-by-atom accuracy. Our developed screening process is extremely fast, allowing us to generate and analyze a database of 5454 low-energy bimetallic NPs. By identifying thermodynamically stable NPs, we rationalize bimetallic mixing at the nanoscale and reveal metal-, size-, and temperature-dependent mixing behavior. Importantly, our method is applicable to any bimetallic NP size, bridging the materials gap in nanoscale simulations, and guides experimentation in the lab by elucidating stability, mixing, and detailed chemical ordering behavior of bimetallic NPs.

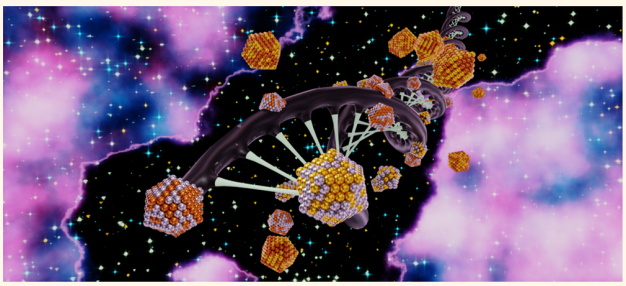

KEYWORDS: *bimetallic nanoparticles, thermodynamic stability, mixing, phase diagram, genetic algorithm, machine learning, density functional theory*

Metal nanoparticles (NPs) are extremely versatile materials, finding applications in a wide variety of fields including catalysis, pigmentation, medicine, and optics.[1] Many of these applications take advantage of structurally dependent properties, by tuning the NP composition, chemical ordering, size, and shape. NP composition (type and ratio of metal atoms) can govern catalytic turnover frequencies,[2] magnetic properties,[3] and electronic structure.[4] Chemical ordering (metal atom distribution within the NP) determines the makeup and location of active catalytic sites,[5] which can greatly affect adsorption energy[6,7] and the stability of the NP itself.[8] NP size (number of metal atoms in the NP) can control optical,[9,10] magnetic,[11] adsorption,[12] and electronic[13] properties. NP shape (the spatial arrangement of atoms) can also control the formation of active chemical sites[12] and adsorption properties.[7] It is the interplay between size, shape, composition, and chemical ordering that gives rise to NP characteristic properties, and controlling these structural features tailors NPs to specific applications.

Structural control at the atomic level has been a long-standing goal in the field of nanotechnology.[14] Although certain types of NPs can be produced with atomic level precision,[15−17] atom-by-atom control tends to be impractical or impossible. As a result, the exact, atomically precise NP structures present under experimental conditions are typically not known. A lot of work has focused on predicting the expected structures computationally by using *ab initio* methods like density functional theory (DFT). These include global optimization studies[18,19] as well as metal segregation analyses, which capture the preference of a heterometal dopant to either mix into the bulk or segregate to the surface of a metal nanomaterial (thus predicting core−shell properties).[20−24] Despite the high accuracy of DFT, the method is only computationally tractable for NPs up to ∼2 nm in diameter, limiting it to a small subset of experimental systems. This is due to the $O(N^3)$ scaling of DFT (for N basis functions),[25] which makes it difficult to perform calculations for systems larger than a few hundred atoms and impractical for systems with thousands of atoms. The computational expense makes DFT a poor choice for the high-throughput screening of NPs (over all expected shapes and sizes). Therefore, approaches that bypass DFT, albeit maintaining a similar accuracy without

Received: February 23, 2020
Accepted: June 9, 2020
Published: June 9, 2020

https://dx.doi.org/10.1021/acsnano.0c01586
ACS Nano 2020, 14, 8171−8180

the computational constraints, are needed to predict experimental NP structures.

To overcome the computational limitations of traditional DFT, several methods have appeared in literature that rapidly determine NP energetics, including density-functional-based tight-binding methods,[26] a semiempirical effective medium theory (EMT),[27] and cluster expansion models.[8,28,29] Recently, Yan *et al.* developed the bond centric (BC) model.[30] As an extension to the square-root bond-cutting (SRB) model,[31] the BC model accurately captures the cohesive energy (CE) and thus the stability of NPs through a sum of half-bond contributions. By capturing the coordination environment and accounting for differences in bond-dissociation energy between metal−metal pairs, the model can be applied to NPs of any size, shape, and metal composition. Importantly, this includes bimetallic NPs, which have a continuous interest as tunable structures for use as catalysts,[32] permanent magnets,[33] and biosensors.[34]

Although the BC model overcomes the size constraints of DFT, enabling screening over any size and shape, it is still no match to simulate the vast configurational space exhibited by bimetallic systems. Consider a bimetallic 55-atom NP with arbitrary structure and chemical formula A_xB_{55-x}. At a given composition, the number of possible chemical orderings is expressed as *55-choose-x*. For example, $A_{21}B_{34}$ would have $\approx 10^{14}$ different chemical orderings despite the constrained size and shape. Although structural degeneracy from symmetry may allow for a slight reduction in the number of possible combinations, it does not reduce the search space by an appreciable amount. In addition, in the case of a bimetallic system with N atoms, where each atom can be one of the two metals, there are up to 2^N NPs of different composition. We note that for smaller systems, symmetry can enable the effective use of brute force methods to screen the configurational space.[35] However, the problem of sample space quickly arises (as shown with our 55-atom example) and only continues to increase with NP size.

Although bimetallic NPs exist within a massive configurational space, not all chemical orderings are expected to exist under experimental conditions. Instead, each of these many possible NPs has an intrinsic thermodynamic preference (*i.e.*, stability, measured by CE), and only the favorable ones are expected to be produced *in situ*. As a result, only a subset of the sample space determines the experimental distribution of bimetallic NPs. Accurate NP structural prediction is imperative for design toward specific applications since small changes in structure sharply affects the physicochemical properties of NPs. Herein, we develop a genetic algorithm (GA)—parametrized by the BC model—that maximizes stability by modifying the chemical ordering of bimetallic NPs of any size, shape, and composition. Taking advantage of the GA's computational speed and efficient sampling of the configurational space, we further validate the BC model by revealing strong agreement between the predicted and experimental structure of a 23,196-atom FePt NP.[36] Furthermore, our optimization framework enables us to directly compare the BC model to EMT.[27] Scaling up our approach, we additionally determine low-energy chemical orderings for 5454 NPs of varying sizes, shapes, and compositions for the bimetallic alloys AgCu, AgAu, and AuCu. The results are then collectively analyzed, enabling us to connect composition and size with nanoscale mixing behavior. Finally, we use our predictions to generate temperature-dependent bimetallic phase diagrams as a function of NP size and composition. Importantly, we introduce a high-throughput screening methodology for the discovery of thermodynamically stable bimetallic nanostructures, applicable to realistic systems, bridging the materials gap between theory and experiment.

RESULTS AND DISCUSSION

We began by benchmarking our GA to assess how rapidly it would find low-energy states. We selected AgCu as a model system since it is known to favor a Cu-core Ag-shell configuration.[37] Utilizing our GA, we benchmarked an icosahedral $Ag_{1234}Cu_{1635}$ NP to see if it would capture the expected core−shell behavior, despite being presented with an extremely large search space ($\approx 10^{849}$ possibilities excluding symmetry). Figure 1 reveals that the GA converges to the

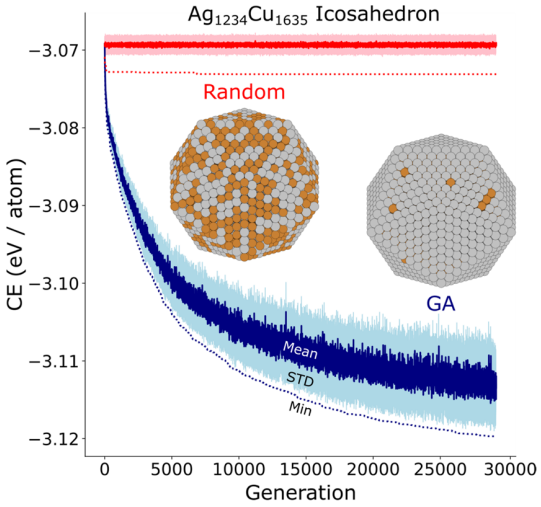

Figure 1. Benchmark of GA performance. We compare GA optimization (blue) against random search (red) on an icosahedral $Ag_{1234}Cu_{1635}$ NP. Darker solid lines and lighter shaded regions represent the mean and standard deviation (STD) of a generation, respectively. Dotted lines indicate the minimum CE found at a given generation. The minimum CE structures are inlaid.

experimentally expected core−shell NP. Furthermore, the GA was able to screen the 1.45×10^6 NPs used for this benchmark at a rate of 70,000 NPs/min on a single core of a typical desktop computer. A random search, having less overhead compared to the GA, screens NPs at a faster rate (≈400,000 NPs/min). However, the speed advantage of random search is undermined by the absence of an optimization scheme, and the approach does not efficiently sample the vast configuration space. This results in a failure to (i) converge to the core−shell mixing behavior expected by experiment and (ii) find chemical orderings as low in energy as those found by the GA (Figure 1).

Consequently, there are clear differences in the surface makeup of the GA-optimized NP and the best NP from random search. Furthermore, although the GA converges to a structure with some Cu atoms on the surface, this does not stem from difficulties in finding the minimum. Rather, this stems from the composition we chose: The subsurface and core atoms are completely filled by Cu, and there is nowhere else to place the remaining Cu atoms but on the surface.

To further gauge the accuracy and scalability of our optimization framework, we next apply our GA to an $Fe_{6569}Pt_{16627}$ NP for which the structure has been exper-

https://dx.doi.org/10.1021/acsnano.0c01586
ACS Nano 2020, 14, 8171−8180

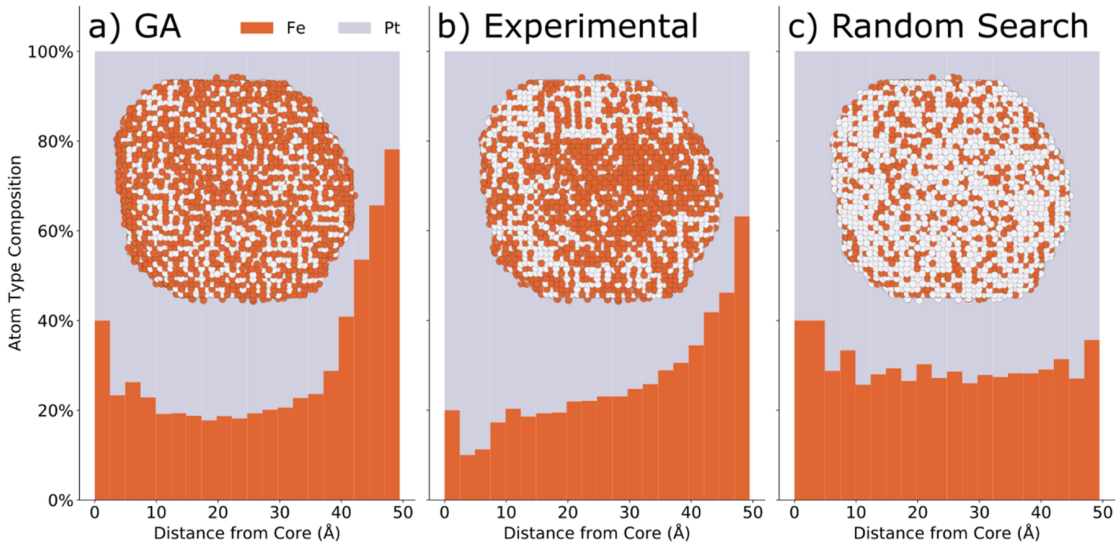

Figure 2. Comparison of different methodologies for identifying optimal chemical ordering. Shown are the structures of (a) the GA-derived $Fe_{6569}Pt_{16627}$ NP to (b) the experimental structure reported by Yang *et al.*[36] and (c) the lowest-energy NP identified *via* random search. Core-centered radial distributions of Fe−Pt composition are represented as bar plots. The NP structures are inlaid.

imentally determined.[36] Through the elemental radial distribution functions shown in Figure 2, we reveal that the GA-optimized NP (Figure 2a) captures the Fe-rich surface and Pt-rich core exhibited in the experimental NP (Figure 2b). It is worth noting that using percent composition exaggerates the composition differences in shells with fewer atoms. For example, in the first shell (radius = 0−2.5 Å), there are five atoms. Because one atom in this shell is different, this is reflected by a 20% difference between this shell's percentage composition and experiment. The differences are less exaggerated in shells with larger number of atoms. For example, in a shell containing 500 atoms, a difference of one atom would be reflected by just 0.2% in composition.

Additionally, we note that the BC model only considers thermodynamic effects. Therefore, slight differences between the GA-optimized and experimental NPs could be attributed to kinetic effects within the large experimental system (*e.g.*, cluster growth, atomic diffusion, mass transfer, *etc*). More important than the radial distribution is, arguably, the distribution of atoms at the surface, where interfacial phenomena (*e.g.*, adsorption and catalysis) occur. Hence, it is important that the methodology accurately captures the surface composition. We observe that the GA produces an excellent prediction of the true experimental surface. The results are in stark contrast to a random search approach (Figure 2c) where we generated many random chemical orderings (sampling the same number of NPs as the GA) and report the most favorable based on their CE. The random NP search completely fails to capture both the radial distribution as well as the surface composition of the experimental NP. Overall, the results demonstrate the success of the GA to effectively sample a massive configurational space of experimental bimetallic NPs. Importantly, we show that our methodology allows for the fast and accurate screening of NPs which are far beyond the reach of DFT.

The screening of bimetallic NPs for their chemical ordering is an emerging field. For example, in 2018 Larsen *et al.*[8] demonstrated the use of mixed integer programming coupled with a semiempirical EMT[27] for the direct optimization of NP chemical ordering. The authors investigated icosahedral 309-atom AgAu NPs, determining the global ground-state chemical ordering for all possible compositions. These EMT global minima provide a data set to directly compare the BC model and assess its effectiveness in capturing optimal mixing behavior. Thus, we used our GA to optimize the same set of NPs. We note that although the GA-optimized NPs are not guaranteed to be global minima (due to the algorithm's stochastic nature), they are expected to be relatively close. We next selected a subset of NPs from both data sets and calculated the excess energy (EE) of each system using DFT. The results, shown in Figure 3, reveal that for every case, our GA-optimized NPs exhibit lower EE (*i.e.*, higher thermodynamic preference to mix) than the global minimum structures from EMT. In addition, we observe differences in the composition predicted to be the minimum in energy. The GA predicts a minimum-energy composition close to 50/50

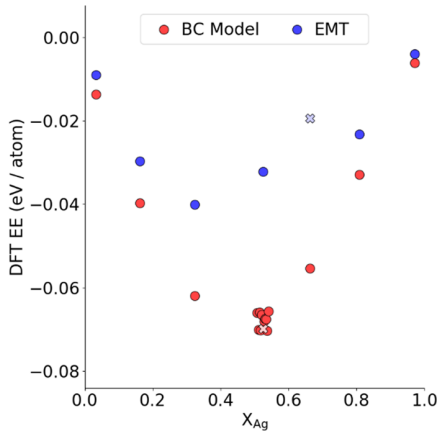

Figure 3. Comparison of different methodologies of optimizing chemical ordering. DFT is used to compare the EE of 309-atom AgAu icosahedral NPs with chemical ordering optimized using EMT (blue) and the BC model (red) at different compositions. X indicates the composition predicted to be of minimum energy by the respective method.

https://dx.doi.org/10.1021/acsnano.0c01586
ACS Nano 2020, 14, 8171−8180

Ag/Au, which shows a strong agreement with DFT calculations. Conversely, EMT deviates from DFT in capturing the correct EE trend and the most favorable composition. To be more confident that the minimum-energy composition is close to 50%, we additionally checked the optimized chemical orderings predicted by our GA near this composition and found that the overall EE trend holds (*i.e.*, most favorable mixing near 50/50 Ag/Au). We note that the results only compare the capabilities of the BC model to EMT and do not make any comparison to the two optimization approaches. Nevertheless, our results prove that, unlike EMT, the BC model correctly captures mixing behavior of AgAu NPs.

Based on our successful results with the predicted structure of the $Fe_{6569}Pt_{23196}$ NP, and the comparison with a recent method of screening NPs for their chemical ordering, we investigated a large variety of bimetallic alloy systems. We investigated the alloys AuCu, AgAu, and AgCu, chosen because they have all been shown to be described well by the BC model.[30] Icosahedrons, cuboctahedrons, and elongated pentagonal bipyramids (EPBs) of up to 3871 atoms (≈4 nm diameter) were investigated. For systems with up to 309 atoms, all possible compositions were investigated. Above this size, compositions were investigated in 10% increments as closely as the chemical formula would allow.

We choose these particular morphologies because they generally result in clusters containing so-called "magic numbers" of atoms (13, 55, 147, *etc*). This is important in the identification of low-energy NP structures, as NPs with magic numbered sizes tend to be of high stability.[38] In addition, we note the synthetic accessibility of these morphologies.[39−41] The EPB structure is particularly relevant to the study of nanowires, which have been demonstrated in Ag to grow *via* a continued elongation of this morphology.[41] Although irregular morphologies such as the $Fe_{6569}Pt_{16627}$ NP (Figure 2) are oftentimes experimentally synthesized, we have demonstrated that our methodology extends well to even these systems as long as a reasonable bond network can be estimated. Hence, our choice of these morphologies should be sufficient to probe the limits of our methodology, as they provide a wide range of possible coordination environments in experimentally relevant nanostructures. Furthermore, their "regular" shape lends itself well to the programmatic generation of reasonable NP structures at any size.

Overall, we report minimum-energy configurations for 5454 different structures. We illustrate a small fraction of the range of structures in Figure 4, where each NP shown is the most stable chemical ordering and composition at the given size, shape, and metal pair. Considering the number of energy calculations required for the GA to converge, and the scaling behavior of DFT (limited to systems of approximately hundreds of metal atoms), this study is computationally infeasible using first-principles methods. In addition, because of the number of possible configurations each NP can assume (ignoring symmetry, 2^N per cluster of N atoms), an exhaustive brute force search of our chosen chemical space is impossible even with the computational speedup provided by the BC model. It is only by combining a computationally inexpensive method (the BC model) with a tried-and-tested optimization technique (GA) that we have the capacity to determine NPs toward global optimum chemical ordering within this tremendous materials space. Based on our results shown in Figure 4, we find an agreement between our algorithm's predictions and literature reports. For example, AgAu NPs

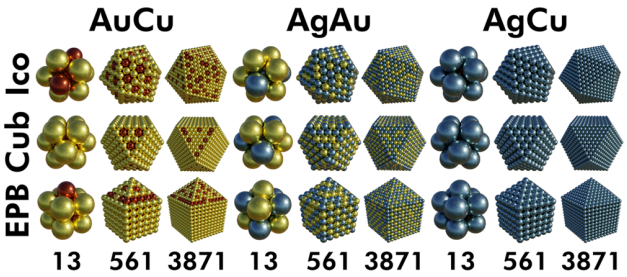

Figure 4. Images of the lowest-energy composition and chemical ordering observed for a sample of the NPs investigated, illustrating the breadth of our study. NPs of size 13, 561, and 3871 atoms are shown. Left three columns: AuCu. Center three columns: AgAu. Right three columns: AgCu. Top row: Icosahedrons. Middle row: Cuboctahedrons. Bottom row: EPBs.

have been produced with both core−shell and homogeneously mixed motifs, however the core−shell structure is metastable due to the tendency for Ag and Au to alloy. Upon a heating−cooling cycle, the thermodynamically stable, homogeneous-mixed AgAu structure emerges,[42] which is generally what our model predicts as the most stable chemical ordering for AgAu NPs of all shapes and sizes. In the case of AgCu, a DFT-based global optimization observed Cu-core/Ag-shell NPs to be the most favorable, which was attributed to the tendency for the two to remain in (and undergo transformation to) an unmixed state in the bulk.[43] This core−shell behavior is exactly what we observe with our GA algorithm. In fact, the most favorable chemical ordering and composition for every shape and size AgCu NP was found to be a perfect Ag-shell Cu-core structure.

Chemical ordering parameters as a function of homoatomic and heteroatomic bond counts have been applied by other groups as a useful tool to uncover mixing trends within bimetallic systems.[37,44,45] However, these parameters usually reduce the bond counts down to a single value to find correlations with structural properties of interest, like size or composition. Instead of distilling the counts down to a single parameter, we developed a visualization of NP mixing. The plots shown in Figure 5 enable us to depict each bond type along with NP size. As an example on creating the plots for a bimetallic NP made of elements A and B, we calculate each bond type (A−A, B−B, and A−B) as a fraction of the total number of bonds (F_{A-A}, F_{B-B}, F_{A-B}). Conveniently, each fraction must be between 0 and 1, and all three must add up to 1 (eq 1).

$$F_{A-A} + F_{B-B} + F_{A-B} = 1 \quad (1)$$

Using our calculated bond fractions, we next build a scatter plot of F_{A-A} *vs* F_{B-B} and rotate the axis such that the origin is at the top of the graph. By leveraging the unity sum constraint of eq 1, we can then draw horizontal lines of constant mixing (*i.e.*, constant values of F_{A-B}). The bottom-most line in the plot would be a completely unmixed system with no heteroatomic bonds, as shown in Figure 5a (labeled "$F_{A-B} = 0$"). At the origin would be a system with no bonds between the same atom type (*i.e.*, only heteroatomic bonds, labeled "$F_{A-B} = 1$" in Figure 5a). As an example, the NP represented as a star in Figure 5a has a heteroatomic bond fraction of 0.4 due to the homoatomic bond fractions (shown with thin dashed lines) of 0.2 and 0.4. Since this representation is normalized by total bond counts, we can plot bimetallic NPs of any size, shape, and

https://dx.doi.org/10.1021/acsnano.0c01586
ACS Nano 2020, 14, 8171−8180

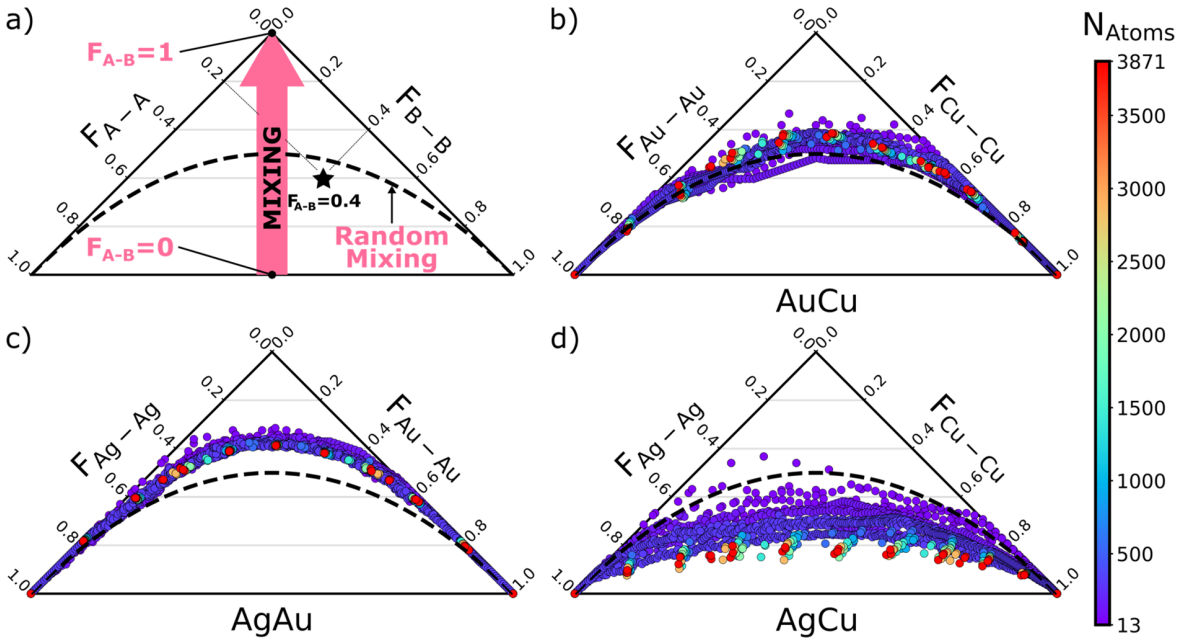

Figure 5. Bond composition plots. (a) Guiding plot illustrating the theoretical mixing limits from no heteroatomic bonds (F_{A-B} = 0) to no homoatomic bonds (F_{A-B} = 1), with a NP example having 40% heteroatomic bonds (star). Light gray lines represent constant mixing (*i.e.*, constant fraction, F, of heteroatomic bonds). The black dashed line indicates a system with fully random mixing (see Supporting Information Section 3 for its derivation). Points on the plots represent (b) AuCu, (c) AgAu, and (d) AgCu NPs at all sizes and compositions studied (5454 total structures), demonstrating the chemical ordering that is thermodynamically preferred. NP sizes are color-coded by number of total metal atoms (N_{Atoms}).

composition on a single plot, enabling global mixing trends to emerge.

Our GA-optimized AuCu, AgAu, and AgCu NP results are presented through bond composition plots in Figure 5b–d. Figure 5c reveals that AgAu exhibits the highest degree of mixing regardless of NP size, which strongly agrees with experimental observations.[37] AuCu systems yield similar results (Figure 5b), although there is a slight influence by the NP size on the mixing behavior, as depicted by the different heights (degree of mixing) of the colored points (different NP sizes). Interestingly, for the AgCu system, Figure 5d illustrates unfavorable mixing behavior, which clearly contrasts with results from the other d^9 metal pairs. These conclusions agree with experimental observations that AgCu NPs tend to minimize the number of heteroatomic bonds *via* obtaining a Cu/Ag core/shell morphology.[43] Overall, we show that mixing is diminished as the AgCu NPs grow in size, which suggests that the degree of mixing can be tuned by controlling NP size. These results can also be analyzed in reference to a "fully random" system, where the bond fractions share equal likelihood and are determined strictly from probability (see Supporting Information Section 3). Using this system as a reference (the dashed line in Figure 5), the results reveal that AgAu NPs favor heteroatomic bonds, while AgCu NPs favor homoatomic bonds.

We note that the trends demonstrated in Figure 5 only show structural trends resulting from the low-energy structures our GA identified within particular alloys and only show whether an alloy is mixed to a lesser or greater degree than a perfectly random alloy (the dashed line in Figure 5). In other words, just because one alloy has a high degree of mixing in these plots does not imply that it is more energetically favorable than another alloy. Instead of rationalizing thermodynamics from structure, we can rationalize structure from thermodynamics. Thermodynamics can be leveraged to rationalize the structural tendency for these materials to either alloy (AgAu and AuCu) or core–shell (AgCu) NPs. In Table 1, we list the DFT-calculated enthalpies of formation for bulk crystal cells of AuCu, AgAu, and AgCu (for simplicity, in each case both metals exist in a 1:1 ratio) reported by the Open Quantum Materials Database (OQMD).[46,47] In cases where the OQMD reports multiple potential structures, we use the one with the most-favorable enthalpy of formation. In our case, energetics (and as a result, structure) at the nanoscale appear to reflect the energetics of the bulk mixing behavior: The AgAu and AuCu bulk alloys listed in Table 1 have favorable formation energies. This indicates that mixing is energetically preferred in bulk and is also what we observe at the nanoscale, and this energetic preference causes the GA to give rise to the structural trends (*i.e.*, preference to mix) we see in Figure 5b,c.

Table 1. Bulk Enthalpies of Formation for AuCu, AgAu, and AgCu[a]

alloy	OQMD entry number	enthalpy of formation (eV/atom)
AuCu	31283	−0.053
AgAu	327735	−0.041
AgCu	307818	+0.111

[a]Data collected from the OQMD[46,47].

In contrast, AgCu has an unfavorable formation energy in bulk (Table 1), which implies segregation and decomposition are energetically preferred at the bulk scale. This energetic preference to unmix is reflected at the nanoscale (Figure 5d) in the structure of the AgCu NPs, which tend to minimize the formation of Ag–Cu bonds. Indeed, it is generally difficult to

https://dx.doi.org/10.1021/acsnano.0c01586
ACS Nano 2020, 14, 8171–8180

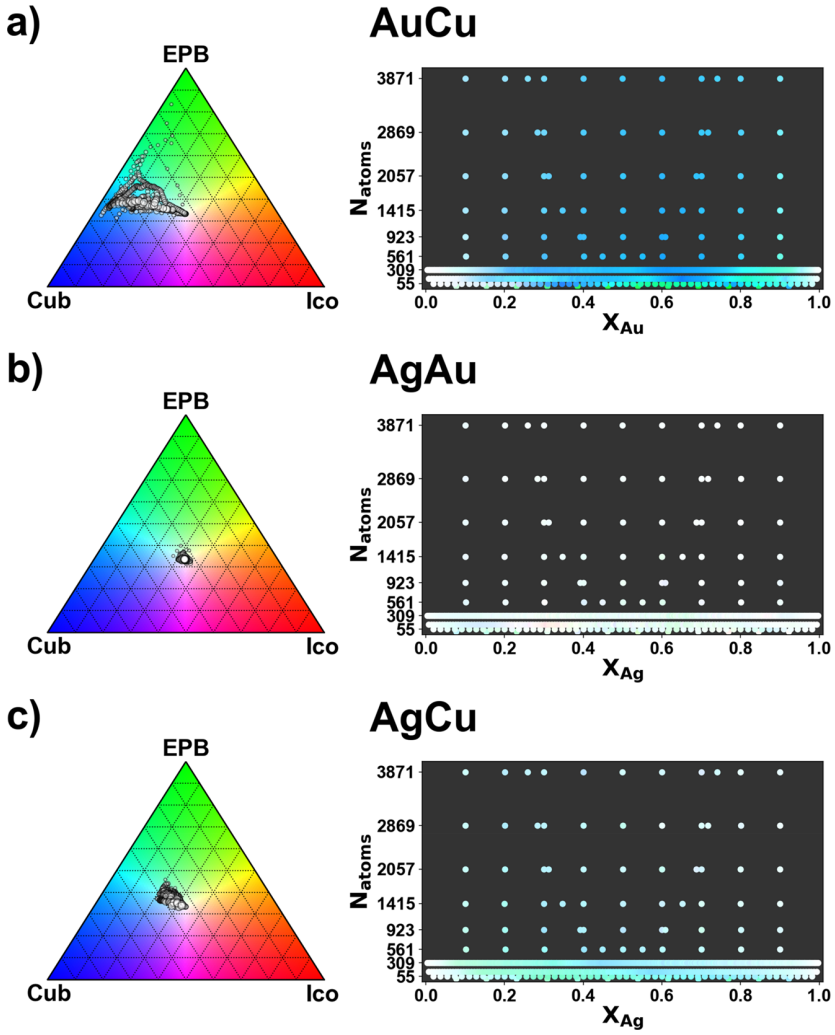

Figure 6. Morphology phase diagrams for the (a) AuCu, (b) AgAu, and (c) AgCu systems at 298 K. The right-hand column plots the preferred morphological phase as a function of the number of atoms and composition of the system. The legend is given by the ternary diagrams on the left-hand side, which show the percentage of the Boltzmann population taking on cuboctahedral, icosahedral, or EPB morphology. White points, for example, indicate all three morphologies are equally favorable. In addition, the size of the points on the ternary diagrams corresponds to NP size.

mix Ag and Cu. In the solid phase, the maximum solubility of Ag in Cu is only 4.9%, and the maximum solubility of Cu in Ag is 14.5%.[48] Alloys which have higher levels of dissolved Ag or Cu are known to exist, but are metastable.[48] Similarly, although AgCu NPs have been produced, they exhibit issues with stability, and spinodal decomposition has been generally observed to occur above 210−230 °C.[49,50] Despite this, the presence of AgCu NPs experimentally reveals the importance of assessing entropy: Their formation must be entropically driven due to their positive enthalpy of formation.

We apply the regular solution approximation, assessing the configurational entropy of mixing as defined in eq 4. We assume that differences in vibrational entropy across NPs of a given alloy will be small enough that they can be neglected, which is supported by test calculations presented in Supporting Information Tables S1 and S2. These results show that at constant size, shape, and composition, changes in chemical ordering result in minimal changes to the vibrational entropy of a NP. Additionally, they show that changes in the composition of these systems result in relatively small changes to the vibrational entropy. Although more accurate methods of approximating NP configurational entropy exist (*e.g.*, using Monte Carlo methods),[51,52] they would add additional computational complexity, prohibiting an analysis at the scale presented (5454 NPs ranging from 13 to 3871 atoms). Moreover, we note that the regular solution approximation is well known to adequately describe NP mixing behavior and phase trends.[53−57] Thus, we use the regular solution assumption (*i.e.*, assume ideal mixing behavior for entropic contributions) as a proof-of-concept to approximate composition and temperature effects of competing morphologies within a given alloy.

By combining configurational entropy and enthalpy, we can evaluate morphological preferences *via* the Gibbs free energy of mixing. From here, we can construct a Boltzmann population (see Computational Methods) of the three morphologies. In Figure 6, we visualize the effect of size and composition on the Boltzmann populations at 298 K. Three morphologies are considered: icosahedral, cuboctahedral, and EPB. There are of course many other morphologies for these

https://dx.doi.org/10.1021/acsnano.0c01586
ACS Nano 2020, 14, 8171−8180

systems beyond those we consider, hence this analysis is primarily intended as a proof-of-concept of our GA's utility in the prediction of nanoscale phase diagrams. Nevertheless, Figure 6 reveals important trends between metal pairs as well as the three morphologies. For instance, although the icosahedral morphology can be a significant fraction of the population, it never seems to be the dominant phase. Instead, whenever there is a dominant set of phases, it is typically the cuboctahedron and EPB in competition with each other, which is shown by the lack of red present in our phase diagrams in Figure 6. Additionally, we observe strong size effects on morphology preference within our results. In all three morphologies, as size grows, a greater fraction of the atoms is fully coordinated in the interior of the NP, and all atoms would be fully coordinated at the limit of an infinitely large NP (*i.e.*, they would converge to the bulk). Since the only difference in coordination between the three geometries occurs at the surface, the three shapes are at their most dissimilar when the ratio of surface atoms is maximized. In other words, when comparing similarly sized systems, differences in energy are at their greatest when the NPs are at their smallest. This is especially prevalent in the AuCu system (Figure 6a), where there is a heavy energetic preference toward EPB at small sizes, gradually converging toward a mix of EPB, cuboctahedron, and icosahedron at larger sizes. Overall, the population-based results presented in Figure 6 provide a more nuanced view than one which only considers the lowest-energy phase to be the dominant one. Importantly, they show that both size and composition play a central role in governing the NP morphology distribution. Furthermore, we investigated the effect of temperature on our Boltzmann populations and report in the Supporting Information variations of Figure 6 calculated at 77 K (Figure S1), 640 K (Figure S2), and 1073 K (Figure S3). These results reveal a rich distribution of structures at higher temperatures, and a stronger preference for specific structures at low temperatures, highlighting the importance of temperature on NP morphology distributions.

CONCLUSIONS

In summary, we have developed a methodology which blends the recently developed BC model[30] with machine learning (GA) for the rapid prediction of stable bimetallic NPs of any size, shape, and metal composition. We demonstrated the speed and accuracy of our GA through a benchmark study optimizing the chemical ordering of a 2869-atom icosahedral AgCu NP. The benchmark shows the effectiveness of the GA in capturing expected experimental trends compared to random guess. We further demonstrated the accuracy and applicability of our approach by predicting the chemical ordering of an experimentally determined $Fe_{6569}Pt_{16627}$ NP, achieving (i) an extremely close radial distribution of the composition and (ii) an accurate prediction of the surface composition of the NP (important for surface science applications, such as catalysis). Using results from our model, we compared the BC model to EMT[27] and demonstrated that the BC model has superior predictive power toward capturing mixing behavior of bimetallic NPs when compared to DFT calculations. Moreover, we predicted the chemical ordering of 5454 bimetallic AuCu, AgAu, and AgCu NPs in a variety of sizes, shapes, and compositions, rationalizing experimental observations. The developed GA code and NP database are available free of charge on GitHub. We introduced a visualization scheme for mixing within a NP, allowing the effective rationalization of mixing behavior between a variety of bimetallic nanostructures (different NP sizes and metal compositions). Using this visualization scheme, we connect mixing behavior to NP size and demonstrate that mixing in AgCu NPs decreases with NP size. In conjunction with Boltzmann statistics, we developed temperature-dependent size-composition phase diagrams for each of the three alloy systems to study the distribution of three competing morphological phases. By investigating a variety of alloy compositions, sizes, and shapes, we demonstrate that our optimization scheme accurately captures low-energy NPs without needing to resort to DFT, with the benefit of being applicable to a broad range of NP sizes (simulating tens of thousands of atoms *vs* several hundred with DFT). Overall, our methodology allows for the identification of stable bimetallic NPs with atomically precise chemical ordering, which is essential for enabling the simulation of realistic, experimentally relevant NPs. As a result, our work advances the elucidation of the bimetallic NP genome.

COMPUTATIONAL METHODS

Density Functional Theory. DFT calculations were performed using CP2K[58] implementing Quickstep.[59] The PBE functional[60] was used (unrestricted Kohn–Sham approach) in conjunction with a DZVP basis set,[61] GTH pseudopotentials[62] with a 500 Ry cutoff, and an SCF convergence within 10^{-8} Ha. A box size of 30 × 30 × 30 Å was applied for all systems. In addition, we utilized Fermi–Dirac smearing with an electronic temperature of 300 K. For vibrational frequency calculations, the Hessian was constructed *via* CP2K's built-in finite difference method with displacements of 0.02 Bohr. Geometries were optimized until forces were below 4.5×10^{-4} Ha/Bohr. In the case of 13- and 55-atom NPs, the energetic minimum was confirmed *via* the lack of imaginary modes in the vibrational analysis. In cases where imaginary vibrational frequencies were observed, a tighter force convergence criterion of 10^{-4} Ha/Bohr was used in conjunction with an SCF convergence criterion of 10^{-9} Ha. If imaginary frequencies remained despite the enhanced convergence criteria, the structure was not considered for further analysis. In all cases, vibrational analysis was performed with an SCF cutoff of 10^{-9} Ha and 0.02 Bohr displacements for the central differencing scheme.

Thermodynamic Properties. CE is conceptually the average bond energy holding a NP or crystal together. Thermodynamically, this can be represented as the energy gained or lost in the separation of all the atoms in a nanocluster to an infinite distance. This is described in eq 2 as the difference in energy of the cluster (with formula A_xB_y) and each separate atom (with single atoms denoted as A_1 and B_1).

$$\mathrm{CE}_{A_xB_y} = \frac{E_{A_xB_y} - (xE_{A_1} + yE_{B_1})}{x + y} \tag{2}$$

EE can be calculated from CE and provides a measure for which we can quantify the tendency of two metals to mix in a NP: The more-negative the EE, the more favorable the mixing.

$$\mathrm{EE} = \mathrm{CE}_{A_xB_y} - \left(\frac{x}{x+y}\mathrm{CE}_{A_{x+y}} + \frac{y}{x+y}\mathrm{CE}_{B_{x+y}}\right) \tag{3}$$

Entropy of mixing ($\Delta S_{\mathrm{mix}A_xB_y}$) is calculated per eq 4.[63] We denote fractional composition *via* X; for example, $X_A = 0.5$ indicates 50% of the atoms in the cluster are of type A, and k_B is Boltzmann's constant.

$$\Delta S_{\mathrm{mix}A_xB_y} = (X_A \log X_A + X_B \log X_B)k_B \tag{4}$$

In Supporting Information Section 1 (Connecting Excess Energy with Enthalpy of Mixing), we show an approximation relating the EE with the enthalpy of mixing (ΔH_{mix}). This approximation allows us to

https://dx.doi.org/10.1021/acsnano.0c01586
ACS Nano 2020, 14, 8171–8180

determine the free energy of mixing (ΔG_{mix}) for any of the A_xB_y systems presented in this work (eq 5).

$$\Delta G_{mix} = \Delta H_{mix} - T\Delta S_{mix} \approx EE - T\Delta S_{mix} \quad (5)$$

Utilizing the free energy of mixing, we calculate the Boltzmann distribution probabilities[64] (p_i) for the presence of the three different shapes studied at a given size, composition, and temperature T (eq 6):

$$p_i = \frac{e^{\Delta G_{mix_i}/k_B T}}{\sum_{j=1}^{3}(e^{\Delta G_{mix_j}/k_B T})} \quad (6)$$

Finally, bond fractions are calculated for a given structure as the percentage of that type of bond relative to all bonds in the system (*e.g.*, C_{A-A} represents the count of A−A bonds). The bond fraction F is calculated *via* eq 7:

$$F_{A-A} = \frac{C_{A-A}}{C_{A-A} + C_{B-B} + C_{A-B}} \quad (7)$$

Genetic Algorithm. To determine the optimal chemical ordering of a bimetallic NP at a given size, shape, and composition, we implemented a GA using Python and C. The GA begins by creating an initial population (generation 0) of 50 bimetallic NPs with random chemical ordering. Each bimetallic NP is represented as a binary array, where zeros correspond to the first atom type in the alphabetized chemical formula (*e.g.*, AgCu would represent Ag as 0, and Cu as 1). As a consequence of these constraints, all arrays have the same length and sum to the same value. To propagate to the next generation, the population is first evaluated for stability using the BC model,[30] given in eq 8:

$$CE_{NP} = \frac{1}{n}\sum_{1}^{m}\left(\gamma_i \frac{CE_{bulk,i}}{\sqrt{CN_i CN_{bulk,i}}} + \gamma_j \frac{CE_{bulk,j}}{\sqrt{CN_j CN_{bulk,j}}}\right) \quad (8)$$

The BC model calculates the CE of a NP with n atoms by summing contributions from all bonds m in the system. Half-bond contributions between atoms i and j are calculated by their respective coordination number (CN), bulk CN (CN_{bulk}), bulk CE (CE_{bulk}), and a weight factor based on gas phase bond dissociation energies (γ). The model was implemented in C, enabling rapid screening of stability for virtually any size bimetallic NP.

Once CE values were calculated for each NP k, fitness scores f were developed using eq 9, where $|CE_{NP}|_{min}$ is the minimum absolute value of CE within the population.

$$f_k = |CE_{NP,k}| - |CE_{NP}|_{min} \quad (9)$$

This scales the fitness scores such that the least stable NP in the population has a fitness of 0. We next used the roulette wheel selection algorithm[65] to determine NP as parents for mating. The probability of NP k (p_k) being selected for mating was based on its fitness score relative to the population, as given in eq 10:

$$p_k = \frac{f_k}{\sum_{i=1}^{n} f_i} \quad (10)$$

To ensure that concentration was constrained, we developed a pairwise crossover algorithm to mate two parents into two NP children (Figure 7).

The approach first finds all positions that do not match between the parents (blue numbers in the parents of Figure 7). Next, a pair of these positions are repeatedly chosen at random until each parent has one of each atom type (0 and 1) selected within the pair (highlighted boxes in Figure 7). The atom types over the selected pair are then swapped between parents. The pair selection and swapping continue until half of the different positions are exchanged. The process results in two children NPs that exhibit chemical ordering traits from both parents. After using the pairwise crossover algorithm to create 49 children (leaving one position in the population to pass on the current most stable NP), 80% of the NPs are mutated. Mutations are achieved by randomly swapping 1s and 0s within a NP. The number of swaps is

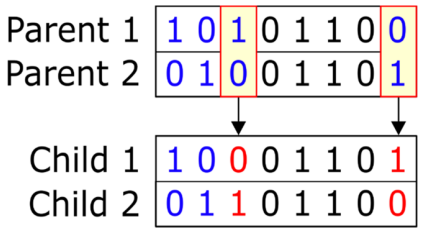

Figure 7. Example of the pairwise crossover algorithm implemented in the GA. Identical positions are in black, while positions with different atom types are in blue. The selected pair within the parents is highlighted in yellow, while the swapped atom types are in red.

calculated using eq 11, where N_0 and N_1 are the number of atom type 0 and 1, respectively.

$$n_{mutation\ swaps} = 0.02 \times \min(N_0, N_1) \quad (11)$$

Employing eq 11 provides a mutation scheme that maintains genetic diversity within the NP population at any size and concentration. After mutation, the fittest NP from the previous population is added to the 49 NPs, completing the population and propelling the GA to the next generation. The overall algorithm continues until the most fit NP remains the same over 2000 generations. At this point, we apply a Metropolis−Hastings algorithm on the most stable NP for 5000 steps in an effort to find a potentially more stable structure with a similar chemical ordering. The resulting minimum CE structure is returned as our GA-optimized NP. Code which implements the GA is available on GitHub (https://github.com/mpourmpakis/ce_expansion). The linked repository includes all required functions for GA simulations as well as functions to visualize and analyze the results. Also included is a python package to build and interface with a SQL database of GA results.

ASSOCIATED CONTENT

Supporting Information

The Supporting Information is available free of charge at https://pubs.acs.org/doi/10.1021/acsnano.0c01586.

Formulation connecting excess energy to enthalpy of mixing, description of statistical thermodynamics used, statistical thermodynamic data derived from DFT for randomly generated 13- and 55-atom AgAu NPs, comparison of alloy NP bond compositions to a fully random bimetallic system, and Boltzmann statistic phase diagrams at various temperatures (PDF)

AUTHOR INFORMATION

Corresponding Author

Giannis Mpourmpakis − *Department of Chemical Engineering, University of Pittsburgh, Pittsburgh, Pennsylvania 15261, United States;* orcid.org/0000-0002-3063-0607; Email: gmpourmp@pitt.edu

Authors

James Dean − *Department of Chemical Engineering, University of Pittsburgh, Pittsburgh, Pennsylvania 15261, United States;* orcid.org/0000-0003-0932-7707

Michael J. Cowan − *Department of Chemical Engineering, University of Pittsburgh, Pittsburgh, Pennsylvania 15261, United States;* orcid.org/0000-0001-8706-782X

Jonathan Estes − *Department of Chemical Engineering, University of Pittsburgh, Pittsburgh, Pennsylvania 15261, United States*

https://dx.doi.org/10.1021/acsnano.0c01586
ACS Nano 2020, 14, 8171−8180

Mahmoud Ramadan − *Department of Chemical Engineering, University of Pittsburgh, Pittsburgh, Pennsylvania 15261, United States*

Complete contact information is available at: https://pubs.acs.org/10.1021/acsnano.0c01586

Author Contributions

†These authors contributed equally.

Notes

The authors declare no competing financial interest.

ACKNOWLEDGMENTS

This work is supported by the National Science Foundation (NSF) under grant no. 1634880 (CMMI) and grant no. 1652694 (CBET-CAREER). M.R. acknowledges support from NSF grant no. 1659324 (REU program). The authors thank the University of Pittsburgh Center for Research Computing (CRC) and the NSF Extreme Science and Engineering Discovery Environment (ACI-1548562) for providing computational resources. Additionally, the authors acknowledge fruitful discussions regarding graph representations of NPs with Prof. M. Stamatakis, from the University College London.

REFERENCES

(1) Stark, W. J.; Stoessel, P. R.; Wohlleben, W.; Hafner, A. Industrial Applications of Nanoparticles. *Chem. Soc. Rev.* **2015**, *44*, 5793−5805.
(2) Renzas, J. R.; Huang, W.; Zhang, Y.; Grass, M. E.; Hoang, D. T.; Alayoglu, S.; Butcher, D. R.; Tao, F.; Liu, Z.; Somorjai, G. A. $Rh_{1-x}Pd_x$ Nanoparticle Composition Dependence in CO Oxidation by Oxygen: Catalytic Activity Enhancement in Bimetallic Systems. *Phys. Chem. Chem. Phys.* **2011**, *13*, 2556−2562.
(3) Shouheng, S.; Fullerton, E. E.; Weller, D.; Murray, C. B. Compositionally Controlled FePt Nanoparticle Materials. *IEEE Trans. Magn.* **2001**, *37*, 1239−1243.
(4) Austin, N.; Ye, J.; Mpourmpakis, G. CO_2 Activation on Cu-Based Zr-Decorated Nanoparticles. *Catal. Sci. Technol.* **2017**, *7*, 2245−2251.
(5) Singh, A. R.; Montoya, J. H.; Rohr, B. A.; Tsai, C.; Vojvodic, A.; Nørskov, J. K. Computational Design of Active Site Structures with Improved Transition-State Scaling for Ammonia Synthesis. *ACS Catal.* **2018**, *8*, 4017−4024.
(6) Dean, J.; Yang, Y.; Austin, N.; Veser, G.; Mpourmpakis, G. Design of Copper-Based Bimetallic Nanoparticles for Carbon Dioxide Adsorption and Activation. *ChemSusChem* **2018**, *11*, 1169−1178.
(7) Dean, J.; Taylor, M. G.; Mpourmpakis, G. Unfolding Adsorption on Metal Nanoparticles: Connecting Stability with Catalysis. *Sci. Adv.* **2019**, *5*, No. eaax5101.
(8) Larsen, P. M.; Jacobsen, K. W.; Schiøtz, J. Rich Ground-State Chemical Ordering in Nanoparticles: Exact Solution of a Model for Ag-Au Clusters. *Phys. Rev. Lett.* **2018**, *120*, 256101.
(9) Lopez, R.; Feldman, L. C.; Haglund, R. F. Size-Dependent Optical Properties of VO_2 Nanoparticle Arrays. *Phys. Rev. Lett.* **2004**, *93*, 177403.
(10) Spanier, J. E.; Robinson, R. D.; Zhang, F.; Chan, S.-W.; Herman, I. P. Size-Dependent Properties of CeO_{2-y} Nanoparticles as Studied by Raman Scattering. *Phys. Rev. B: Condens. Matter Mater. Phys.* **2001**, *64*, 245407.
(11) Lin, X. M.; Sorensen, C. M.; Klabunde, K. J.; Hajipanayis, G. C. Control of Cobalt Nanoparticle Size by the Germ-Growth Method in Inverse Micelle System: Size-Dependent Magnetic Properties. *J. Mater. Res.* **1999**, *14*, 1542−1547.
(12) Taylor, M. G.; Austin, N.; Gounaris, C. E.; Mpourmpakis, G. Catalyst Design Based on Morphology- and Environment-Dependent Adsorption on Metal Nanoparticles. *ACS Catal.* **2015**, *5*, 6296−6301.
(13) Kennedy, M. K.; Kruis, F. E.; Fissan, H.; Mehta, B. R.; Stappert, S.; Dumpich, G. Tailored Nanoparticle Films from Monosized Tin Oxide Nanocrystals: Particle Synthesis, Film Formation, and Size-Dependent Gas-Sensing Properties. *J. Appl. Phys.* **2003**, *93*, 551−560.
(14) Feynman, R. P. There's Plenty of Room at the Bottom. *Eng. Sci.* **1960**, *23*, 22−36.
(15) Jin, R.; Zeng, C.; Zhou, M.; Chen, Y. Atomically Precise Colloidal Metal Nanoclusters and Nanoparticles: Fundamentals and Opportunities. *Chem. Rev.* **2016**, *116*, 10346−413.
(16) Cowan, M. J.; Mpourmpakis, G. Structure−Property Relationships on Thiolate-Protected Gold Nanoclusters. *Nanoscale Adv.* **2019**, *1*, 184−188.
(17) Taylor, M. G.; Mpourmpakis, G. Thermodynamic Stability of Ligand-Protected Metal Nanoclusters. *Nat. Commun.* **2017**, *8*, 15988.
(18) Rapetti, D.; Ferrando, R. Density Functional Theory Global Optimization of Chemical Ordering in AgAu Nanoalloys. *J. Alloys Compd.* **2019**, *779*, 582−589.
(19) Isenberg, N. M.; Taylor, M. G.; Yan, Z.; Hanselman, C. L.; Mpourmpakis, G.; Gounaris, C. E. Identification of Optimally Stable Nanocluster Geometries *via* Mathematical Optimization and Density-Functional Theory. *Mol. Syst. Des. Eng.* **2020**, *5*, 232−244.
(20) Mamatkulov, M.; Yudanov, I. V.; Bukhtiyarov, A. V.; Prosvirin, I. P.; Bukhtiyarov, V. I.; Neyman, K. M. Pd Segregation on the Surface of Bimetallic PdAu Nanoparticles Induced by Low Coverage of Adsorbed CO. *J. Phys. Chem. C* **2019**, *123*, 8037−8046.
(21) Farsi, L.; Deskins, N. A. First Principles Analysis of Surface Dependent Segregation in Bimetallic Alloys. *Phys. Chem. Chem. Phys.* **2019**, *21*, 23626−23637.
(22) Yu, Y.; Xiao, W.; Wang, J.; Wang, L. Understanding the Surface Segregation Behavior of Transition Metals on Ni(111): A First-Principles Study. *Phys. Chem. Chem. Phys.* **2016**, *18*, 26616−26622.
(23) Wang, L.-L.; Johnson, D. D. Predicted Trends of Core−Shell Preferences for 132 Late Transition-Metal Binary-Alloy Nanoparticles. *J. Am. Chem. Soc.* **2009**, *131*, 14023−14029.
(24) Ruban, A. V.; Skriver, H. L.; Nørskov, J. K. Surface Segregation Energies in Transition-Metal Alloys. *Phys. Rev. B: Condens. Matter Mater. Phys.* **1999**, *59*, 15990−16000.
(25) Sousa, S. F.; Fernandes, P. A.; Ramos, M. J. General Performance of Density Functionals. *J. Phys. Chem. A* **2007**, *111*, 10439−10452.
(26) Cuny, J.; Tarrat, N.; Spiegelman, F.; Huguenot, A.; Rapacioli, M. Density-Functional Tight-Binding Approach for Metal Clusters, Nanoparticles, Surfaces and Bulk: Application to Silver and Gold. *J. Phys.: Condens. Matter* **2018**, *30*, 303001.
(27) Jacobsen, K. W.; Stoltze, P.; Nørskov, J. K. A Semi-Empirical Effective Medium Theory for Metals and Alloys. *Surf. Sci.* **1996**, *366*, 394−402.
(28) Sanchez, J. M. Cluster Expansion and the Configurational Theory of Alloys. *Phys. Rev. B: Condens. Matter Mater. Phys.* **2010**, *81*, 224202.
(29) Laks, D. B.; Ferreira, L. G.; Froyen, S.; Zunger, A. Efficient Cluster Expansion for Substitutional Systems. *Phys. Rev. B: Condens. Matter Mater. Phys.* **1992**, *46*, 12587−12605.
(30) Yan, Z.; Taylor, M. G.; Mascareno, A.; Mpourmpakis, G. Size-, Shape-, and Composition-Dependent Model for Metal Nanoparticle Stability Prediction. *Nano Lett.* **2018**, *18*, 2696−2704.
(31) Tománek, D.; Mukherjee, S.; Bennemann, K. H. Simple Theory for the Electronic and Atomic Structure of Small Clusters. *Phys. Rev. B: Condens. Matter Mater. Phys.* **1983**, *28*, 665−673.
(32) Kim, D.; Xie, C.; Becknell, N.; Yu, Y.; Karamad, M.; Chan, K.; Crumlin, E. J.; Nørskov, J. K.; Yang, P. Electrochemical Activation of CO_2 through Atomic Ordering Transformations of AuCu Nanoparticles. *J. Am. Chem. Soc.* **2017**, *139*, 8329−8336.
(33) Sun, S.; Murray, C. B.; Weller, D.; Folks, L.; Moser, A. Monodisperse FePt Nanoparticles and Ferromagnetic FePt Nanocrystal Superlattices. *Science* **2000**, *287*, 1989.
(34) Mandal, R.; Baranwal, A.; Srivastava, A.; Chandra, P. Evolving Trends in Bio/Chemical Sensor Fabrication Incorporating Bimetallic Nanoparticles. *Biosens. Bioelectron.* **2018**, *117*, 546−561.

(35) Rao, Y.; Lei, Y.; Cui, X.; Liu, Z.; Chen, F. Optical and Magnetic Properties of Cu-Doped 13-Atom Ag Nanoclusters. *J. Alloys Compd.* **2013**, *565*, 50−55.
(36) Yang, Y.; Chen, C. C.; Scott, M. C.; Ophus, C.; Xu, R.; Pryor, A.; Wu, L.; Sun, F.; Theis, W.; Zhou, J.; Eisenbach, M.; Kent, P. R.; Sabirianov, R. F.; Zeng, H.; Ercius, P.; Miao, J. Deciphering Chemical Order/Disorder and Material Properties at the Single-Atom Level. *Nature* **2017**, *542*, 75−79.
(37) Ferrando, R.; Jellinek, J.; Johnston, R. L. Nanoalloys: From Theory to Applications of Alloy Clusters and Nanoparticles. *Chem. Rev.* **2008**, *108*, 845−910.
(38) Shevchenko, V. Y.; Madison, A. E. Structure of Nanoparticles: I. Generalized Crystallography of Nanoparticles and Magic Numbers. *Glass Phys. Chem.* **2002**, *28*, 40−43.
(39) Zhang, Q.; Xie, J.; Yang, J.; Lee, J. Y. Monodisperse Icosahedral Ag, Au, and Pd Nanoparticles: Size Control Strategy and Superlattice Formation. *ACS Nano* **2009**, *3*, 139−148.
(40) Radi, A.; Pradhan, D.; Sohn, Y.; Leung, K. T. Nanoscale Shape and Size Control of Cubic, Cuboctahedral, and Octahedral Cu−Cu_2O Core−Shell Nanoparticles on Si(100) by One-Step, Templateless, Capping-Agent-Free Electrodeposition. *ACS Nano* **2010**, *4*, 1553−1560.
(41) Jones, R.; Draheim, R.; Roldo, M. Silver Nanowires: Synthesis, Antibacterial Activity and Biomedical Applications. *Appl. Sci.* **2018**, *8*, 673.
(42) Lewis, E. A.; Slater, T. J. A.; Prestat, E.; Macedo, A.; O'Brien, P.; Camargo, P. H. C.; Haigh, S. J. Real-Time Imaging and Elemental Mapping of AgAu Nanoparticle Transformations. *Nanoscale* **2014**, *6*, 13598−13605.
(43) Bochicchio, D.; Ferrando, R. Size-Dependent Transition to High-Symmetry Chiral Structures in AgCu, AgCo, AgNi, and AuNi Nanoalloys. *Nano Lett.* **2010**, *10*, 4211−4216.
(44) Batista, K. E. A.; Da Silva, J. L. F.; Piotrowski, M. J. Adsorption of CO, NO, and H_2 on the Pd_nAu_{55-n} Nanoclusters: A Density Functional Theory Investigation within the van der Waals D3 Corrections. *J. Phys. Chem. C* **2019**, *123*, 7431−7439.
(45) Lopez, G. E.; Freeman, D. L. A Study of Low Temperature Heat Capacity Anomalies in Bimetallic Alloy Clusters Using J-Walking Monte Carlo Methods. *J. Chem. Phys.* **1993**, *98*, 1428−1435.
(46) Saal, J. E.; Kirklin, S.; Aykol, M.; Meredig, B.; Wolverton, C. Materials Design and Discovery with High-Throughput Density Functional Theory: The Open Quantum Materials Database (OQMD). *JOM* **2013**, *65*, 1501−1509.
(47) Kirklin, S.; Saal, J. E.; Meredig, B.; Thompson, A.; Doak, J. W.; Aykol, M.; Rühl, S.; Wolverton, C. The Open Quantum Materials Database (OQMD): Assessing the Accuracy of DFT Formation Energies. *Npj Comput. Mater.* **2015**, *1*, 15010.
(48) Subramanian, P. R.; Perepezko, J. H. The Ag-Cu (Silver-Copper) System. *J. Phase Equilib.* **1993**, *14*, 62−75.
(49) Sopoušek, J.; Zobač, O.; Buršík, J.; Roupcová, P.; Vykoukal, V.; Brož, P.; Pinkas, J.; Vřešťál, J. Heat-Induced Spinodal Decomposition of Ag−Cu Nanoparticles. *Phys. Chem. Chem. Phys.* **2015**, *17*, 28277−28285.
(50) Sopousek, J.; Pinkas, J.; Broz, P.; Bursik, J.; Vykoukal, V.; Skoda, D.; Styskalik, A.; Zobac, O.; Vrest'al, J.; Hrdlicka, A.; Simbera, J. Ag-Cu Colloid Synthesis: Bimetallic Nanoparticle Characterisation and Thermal Treatment. *J. Nanomater.* **2014**, *2014*, 1−13.
(51) Davari, S. A.; Mukherjee, D. Kinetic Monte Carlo Simulation for Homogeneous Nucleation of Metal Nanoparticles during Vapor Phase Synthesis. *AIChE J.* **2018**, *64*, 18−28.
(52) Reich, M.; Becker, U. First-Principles Calculations of the Thermodynamic Mixing Properties of Arsenic Incorporation into Pyrite and Marcasite. *Chem. Geol.* **2006**, *225*, 278−290.
(53) Guisbiers, G.; Khanal, S.; Ruiz-Zepeda, F.; Roque de la Puente, J.; José-Yacaman, M. Cu−Ni Nano-Alloy: Mixed, Core−Shell or Janus Nano-Particle? *Nanoscale* **2014**, *6*, 14630−14635.
(54) Shirinyan, A. S.; Wautelet, M. Phase Separation in Nanoparticles. *Nanotechnology* **2004**, *15*, 1720−1731.
(55) Jayaganthan, R.; Chow, G. M. Thermodynamics of Surface Compositional Segregation in Ni−Co Nanoparticles. *Mater. Sci. Eng., B* **2002**, *95*, 116−123.
(56) Vallée, R.; Wautelet, M.; Dauchot, J. P.; Hecq, M. Size and Segregation Effects on the Phase Diagrams of Nanoparticles of Binary Systems. *Nanotechnology* **2001**, *12*, 68−74.
(57) Christensen, A.; Stoltze, P.; Norskov, J. K. Size Dependence of Phase Separation in Small Bimetallic Clusters. *J. Phys.: Condens. Matter* **1995**, *7*, 1047−1057.
(58) Hutter, J.; Iannuzzi, M.; Schiffmann, F.; VandeVondele, J. CP2K: Atomistic Simulations of Condensed Matter Systems. *Wiley Interdiscip. Rev. Comput. Mol. Sci.* **2014**, *4*, 15−25.
(59) VandeVondele, J.; Krack, M.; Mohamed, F.; Parrinello, M.; Chassaing, T.; Hutter, J. QUICKSTEP: Fast and Accurate Density Functional Calculations Using a Mixed Gaussian and Plane Waves Approach. *Comput. Phys. Commun.* **2005**, *167*, 103−128.
(60) Perdew, J. P.; Burke, K.; Ernzerhof, M. Generalized Gradient Approximation Made Simple. *Phys. Rev. Lett.* **1996**, *77*, 3865−3868.
(61) VandeVondele, J.; Hutter, J. Gaussian Basis Sets for Accurate Calculations on Molecular Systems in Gas and Condensed Phases. *J. Chem. Phys.* **2007**, *127*, 114105.
(62) Goedecker, S.; Teter, M.; Hutter, J. Separable Dual-Space Gaussian Pseudopotentials. *Phys. Rev. B: Condens. Matter Mater. Phys.* **1996**, *54*, 1703−1710.
(63) Kittel, C. *Introduction to Solid State Physics*, 8th ed.; Wiley: Hoboken, NJ, 2005; p 680.
(64) McQuarrie, D. A. *Statistical Mechanics*; University Science Books: Sausalito, CA, 2000; p 72.
(65) Back, T. *Evolutionary Algorithms in Theory and Practice: Evolution Strategies, Evolutionary Programming, Genetic Algorithms*; Oxford University Press, Inc.: New York, NY, 1996; p 118.

https://dx.doi.org/10.1021/acsnano.0c01586
ACS Nano 2020, 14, 8171−8180